Motion Hypothesis Satellite Detection for Cislunar Spacecraft

Kaitlyn Raub, Tim Mclaughlin
InTrack Radar Technologies, Inc.
Nathan Holzrichter, Stefan Doucette
MITRE Corporation
Francis Chun
United States Air Force Academy

ABSTRACT

Over the next several years, an increase of scientific, commercial, and military missions will be driving a dramatic rise in cislunar traffic. Whereas missions beyond geosynchronous orbit were previously limited to a select few nations, lowered costs and increased demand are causing a wide variety of nations' space programs and commercial entities to visit the Moon, including some spacecraft with humans on board! Cislunar space poses a host of new challenges with regards to Space Situational Awareness (SSA) and Spaceflight Traffic Safety. Complex gravitational dynamics caused by the Moon, Earth, and Sun that allow for low-energy trajectories which rapidly reduce predictability and expand the volume of space requiring surveillance. Further, the vast ranges associated with objects in cislunar space exacerbate sensor sensitivity challenges. Recent work to adapt traditional observing procedures to cislunar ranges has been developed, tested, and deployed, allowing existing ground-based, small aperture optical observatories the ability to track, detect, and image cislunar objects (See Raub 2023, Raub 2022). While these techniques enable observers to update the state of known satellites, the next step in applying existing terrestrial sensors to cislunar SSA is to develop methods for the discovery of unknown or lost objects.

This report details the results of the application of an asteroid detection algorithm to both decrease the required target signal and perform un-cued discovery for cislunar spacecraft. The algorithm is tested utilizing data collected from the Pine Park Observatory (PPO) and the United States Air Force Academy's Falcon Telescope Network (FTN).

1. INTRODUCTION

For the first time since the Apollo program of the 1970's, mankind is looking up towards the skies with renewed hope and excitement as human presence returns to the Moon and beyond. Assisting with this movement is the successful beginning of the Commercial Lunar Payload Services (CLPS) initiative which partners government and commercial space exploration organizations for the first time [1]. Additionally, the first segment of the Artemis program successfully launched in November 2022 as it traversed to the Moon and back with the purpose of testing and preparing the Orion spacecraft and Space Launch Systems (SLS) rocket to safely land humans on the lunar surface in coming years [2].

As the number of satellites in space has grown steadily, so too has the importance and challenge in accurately maintaining positional awareness of those orbiting bodies. To protect scientific assets, commercial investments, and human life in all orbit regimes, the task to continually detect, track, and maintain custody of spacecraft now includes an expanding population of objects orbiting the Moon. Due to the nature of cislunar space, traditional Space Situational Awareness (SSA) methods to first predict the locations of satellites, then detect them, are pushed to their limits and, in many cases, are rendered unusable. Unlike nearer orbits, where the Earth's gravity dominates and orbital trajectories more closely resemble conic sections, space beyond geosynchronous orbit (GEO) is home to chaotic and asymmetrical orbits caused by the combined gravitational effects of the Sun, Moon, and Earth. Compounding the challenge is the increased distances, roughly 10 times greater than GEO [3], which significantly degrades the signal strength.

In orbits extending through GEO, Earth is the dominating gravitational force where the Sun and Moon's effects are considered negligible. Satellite orbits have historically been represented using two-line element sets (TLEs) which are

a list of encoded orbital parameters that describe the motion of an Earth-orbiting spacecraft [4]. Due to the gravitational effects of the Moon and Sun having a greater influence on cislunar spacecraft and cannot be considered negligible, TLEs which have been used for the last few decades are now unusable for describing cislunar objects.

The distances to cislunar objects are an order of magnitude greater than objects in GEO and the volume of space three orders of magnitude greater. This creates a series of challenges when attempting to image cislunar spacecraft due to a sensitivity loss for optical sensors that follows the inverse square law (e.g., an object twice as far is 4x more difficult to detect). Additionally, there's a conic volume of space carved out by the lunar glare that causes difficulty in detecting spacecraft without optical sensors becoming oversaturated from the brightness of the Moon. These are just some of the challenges that observers are faced with when attempting to track, detect, and image cislunar spacecraft.

To address some of the aforementioned challenges, recent work has been developed, tested, and deployed to ground-based, small-aperture optical observatories that adapted traditional observing procedures to cislunar space, allowing them to track, detect, and image known cislunar objects [5], [6]. Attention has since shifted towards the discovery of cislunar objects in imagery without a priori information provided about the object. There is currently neither a database nor a catalog of cislunar objects, which will be necessary to establish and maintain for upcoming missions. This is an important next step in developing a complete SSA process for cislunar objects, and is a target for this research.

The datasets used in this paper were generated using ground-based optical observatories located in Colorado Springs, Colorado, including the Pine Park Observatory (PPO) and the United States Air Force Academy's (USAFA) Falcon Telescope Network (FTN). PPO consists of 0.27-meter aperture while the FTN observatory used utilizes a 16-inch telescope.

The telescope images used for algorithm testing were collected using a sidereal tracking mode to keep stars stationary across the sequence of images. Images were aligned in post-processing to fix any tracking anomalies, hot pixels were removed, and a background flattening process was applied. The images were taken using varying exposures depending on the target object, with the main consideration being to take the longest exposure possible without the object streaking. Additionally, the total time of the sequence of images was long enough to allow for enough relative angular movement for differences in position to be detected. See past work described in *"XGEO Spacecraft Observation Methods Using Ground-Based Optical Telescopes"* for more details on cislunar observation techniques.

2. ALGORITHM OVERVIEW

The algorithm implemented in this research is based on *"Automatic Detection Algorithm for Small Moving Objects"* [7]. While the original algorithm was intended for detecting Near-Earth Objects (NEO), namely asteroids and comets, there are several similarities in the challenges involved in detecting NEOs and in detecting man-made spacecraft in cislunar orbit. In general, NEOs and man-made spacecraft are dim, slow-moving objects relative to observers on Earth.

Our process produces visual graphics and tables for an observer use to locate the position of the target. The first graphic is a set of motion hypothesis plots for each velocity shift used as shown in Fig. 1 below. This initial graphic displays the pixels above a signal-to-noise (SNR) threshold that are extracted with a convolution filter after the background subtraction of stars is completed and several consecutive images are combined to increase the signal of any remaining targets. In the cislunar image results shown later in this paper, we expect target motion to be approximately 1-2-pixels per image given the slow object motion. We're using 1-2-pixel shifts per image due to a priori knowledge of how cislunar targets move between frames given how the data was collected based on exposure times and the collection windows. This bounds the search space required for cislunar spacecraft. Asteroids, however, will require longer exposure, collection windows, and a larger velocity space search as shown in the later data results of this report.

In developing our processing pipeline, we used these plots to distinguish genuine targets from noise. In our tests, genuine targets showed up in multiple X-Y Shift hypotheses – this is enabled by using such small shift values, on the order of several pixels in both the X and Y direction. Manually identifying targets can be further aided by color-coding these plots based on post-convolution pixel intensity, or color-coding the pixel detections by time order.
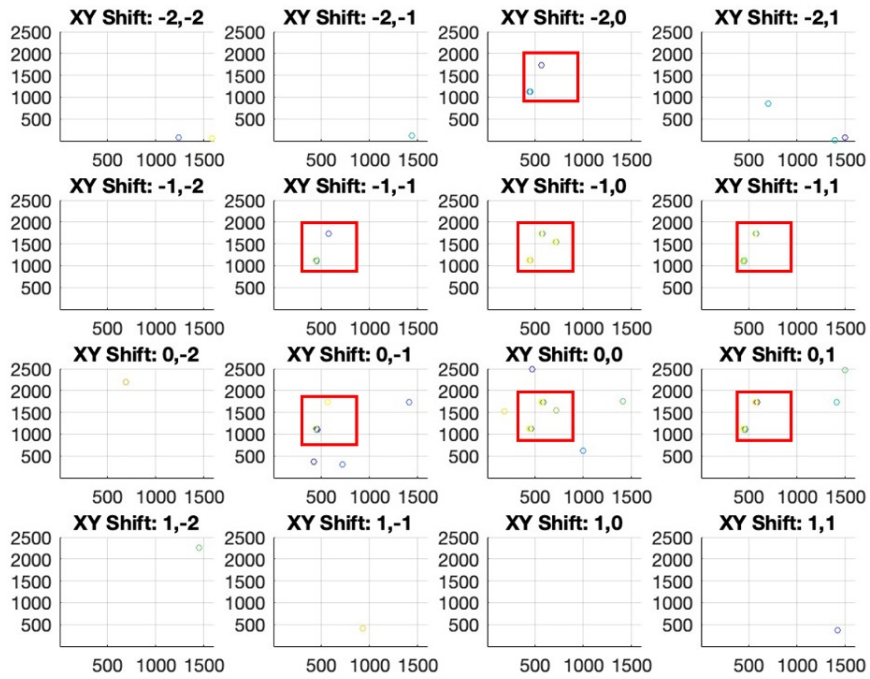
Fig. 1: The first graphic that the algorithm outputs is shown above. This shows detections from the stacks of images that are shifted at differing velocities. Repeating detections are outlined using the red square. Any remaining detections can be attributed to noise.

The second graphic produced takes the detections from the previous stage and groups them into clusters as shown below in Fig. 2. At this stage, we are looking for clusters that are moving in ways that follow the logic of spacecraft trajectories where detections should group together to form a track. Some noise, such as hot pixels that were not removed, do not produce enough pixels in the same area to qualify as a cluster and are consequently ignored.
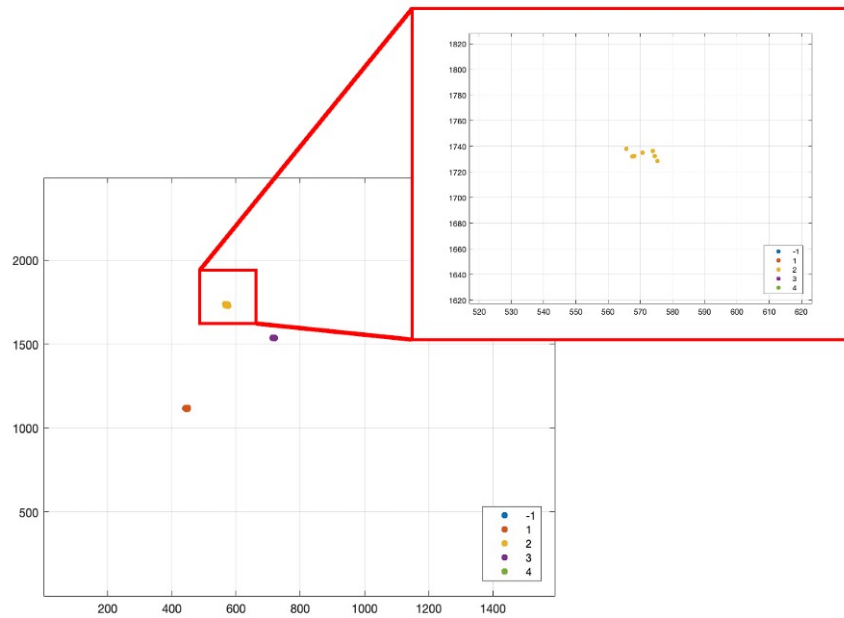
Fig. 2: The second graphic produced shows detection clusters as shown here, along with a zoomed in view of the top target. We can see that the detections are moving in a way that represents a typical spacecraft track that is relatively straight throughout the field of view.

The final visual indicator the algorithm generates overlays the detection clusters shown above to the pixel positions in the original input images. This method allows for visual confirmation that the detections are grouped around an actual target as seen in Fig. 3.
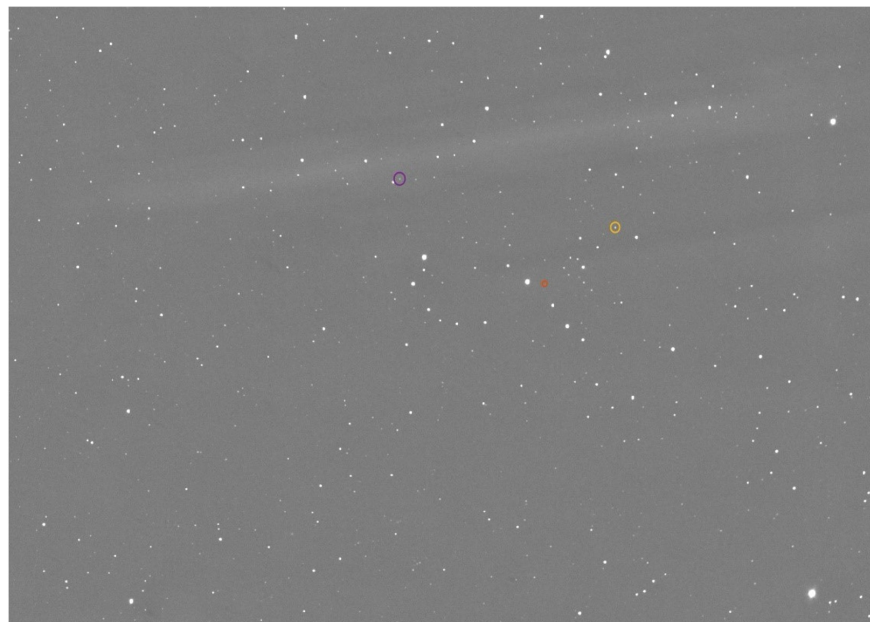

Fig. 3: The detection clusters from Fig. 2 above are shown overlaid on the original images circling the target they correlate to. This provides additional confirmation that the detections associate to a target.

Finally, the algorithm outputs a text file containing the original image number, a group identifier correlating to a cluster of detections, and the mean X and Y pixel location of the detection. This is a list of the targets the algorithm detected from the image sequence.

Our detection process closely follows the algorithm described in *Automatic Detection Algorithm for Small Moving Objects* up to the target candidate search after the first round of image shifting and combining. Whereas *Automatic Detection Algorithm for Small Moving Objects* suggests using larger image shift values followed by refining shift values around target candidates, our process starts with fine shift values and then performs several steps of target detection using pixel signal strength and the size and shape of pixel groups. The shift value search space – the range of expected target motions – is a function of the target trajectory in relation to the interval between collected images. While small shift values worked well in our tests, an analysis of expected object motions should be performed to determine, in conjunction with a specific sensor's operating procedures, the required range of shifting. If this range is large, a two-stage coarse shift strategy with subsequent shift refinement, such as described in *Automatic Detection Algorithm for Small Moving Objects* may be required to keep the computer processing requirements tractable. Lastly, the last two steps of the original algorithm go into celestial coordinate determination and photometric extraction which we ignored in this work. Our intention is not to calculate state vectors or target magnitudes, but to detect targets within imagery without prior knowledge of their position.

The values in Table 1 constitute inputs into our processing pipeline. Ideally, these values would work well over a range of circumstances thereby maximizing target detection with minimal human oversight. Our experimentation found a small range of values that worked well; however, this should be an area of further investigation, particularly when using data from new sensors.

Table 1: Algorithm input values are listed with typical values used within this study.

Input Value	Typical Value Range
The number of images used to create a mask image	50
The location near the center of all images with few or no stars	NA
The range of X-Y pixel shift	-2:2
Standard deviation multiplier to blank out remaining sources in mask image	4
The number of images accumulated into a sub-image	20
The pixel size and shape of the Laplacian of Gaussian filter used to detect targets	7 pixels with standard deviation of 1.83
Target SNR minimum	6
DBSCAN epsilon search radius and minimum number of points for detections across all shift values	Epsilon of 4 and minimum of 4 points

3. ALGORITHM TESTING

3.1 SYNTHETIC IMAGES

Synthetic data was generated using an in-house MATLAB script to generate images that approximate images taken from real sensors. This allowed controlled experiment on some of the individual steps of the target detection process. In the synthetic images, stars were inserted at random pixel positions and intensities. The star image is generated by multiplying a two-dimensional Gaussian distribution by the intensity then adding it to the image at the specified location. Satellites were added in a similar process by randomizing their pixel positions and intensities. To simulate a set of images representing a satellite track from a sensor, the synthetic satellite was given linear motion across the sequence of images. Satellite motion was measured in pixel per image thereby abstracting the time dimension from this process. Additionally, noise was added across the image using a normal distribution.

The synthetic images were first used to demonstrate an increase of a target's signal when a motion hypothesis is applied as shown in Fig. 4 below. Five targets (circled in green) were generated in a sequence of images where the brightness of the targets was varied with target 1 being the dimmest and target 5 being the brightest. The targets were set to move downward at a specified rate over the sequence of images. In the image on the left, no motion hypothesis was applied to the sequence so that the SNR of the target when combined is smeared. The image on the right shows the effects of adding in the correct motion hypothesis to stack the target signal perfectly across the sequence which provided a
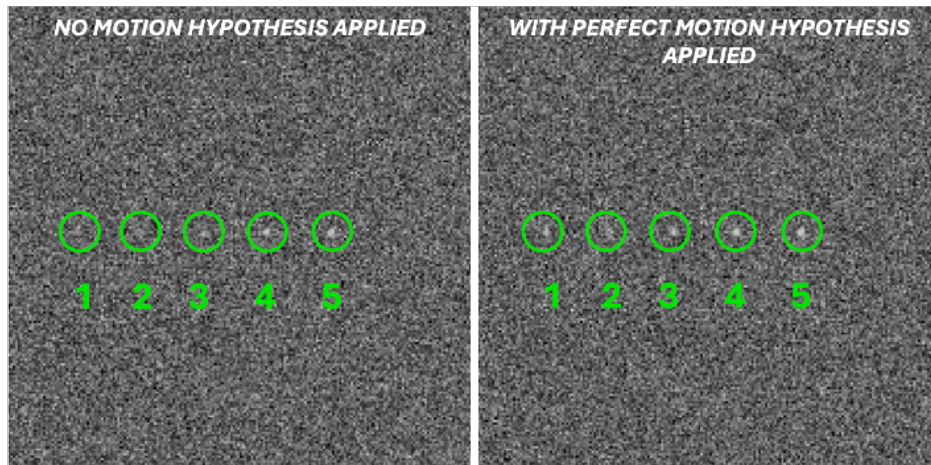
visible improvement signal increase.

Fig. 4: Comparison of performance improvements for application of perfect motion shifts.

3.2 IMPERFECT SHIFTING

Sequences of synthetic images with several targets, as seen above in Fig. 4, can be made where each of the targets move at different rates, measured in pixels/image. These images can then be shifted and combined – taking the median pixel value of each image as per the algorithm – and the resulting target intensity measured as a function of each target's rate of movement. The images are shifted in both the X and Y direction at some increment of integer pixel. In this way the effect of properly matching the target shift rate can be observed.

In Fig. 5 below, the intensity of five targets is measured after shifting and combining a sequence of five consecutive images. The intensity is measured as the ratio of the target's central pixel's value to the standard deviation of the image noise. In this image, motion difference is the magnitude of the vector magnitude difference between the image shifting vector and each targets' motion vector. Whereas shifting the image in perfect congruence with the target motion results in a target magnitude approximately 4 standard deviations above the noise of the image, if the shifting motion is off by one pixel per image a target with the same original intensity is only one standard deviation above the noise of the image. This example demonstrates that the shifting and combining algorithm produce an improved target signal as a function of the congruence of the target motion with the shifting motion.
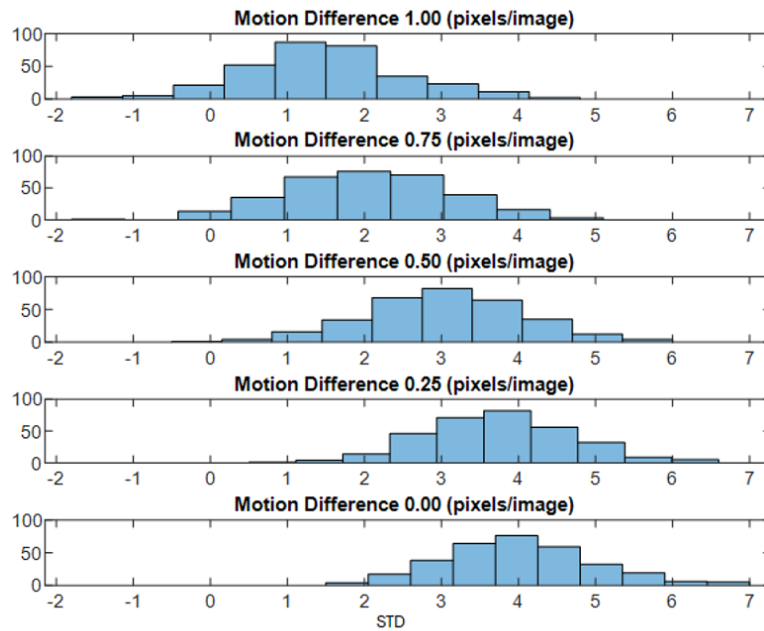
Fig. 5: The intensity of five targets, each target moving at a different rate, demonstrate the intensity of the target after shifting and combining several images as a function of the congruence of the shift motion and the target motion.

3.3 CISLUNAR SATELLITE DATA

The first sensor data presented here consists of cislunar spacecraft image sets.

QUEQIAO-2

Queqiao-2 is a Chinese relay satellite in lunar orbit which provides communication support to multiple Chang'e missions [8]. During the time of the observations, the satellite was accompanied by the associated Chang'e Zheng-8 (CZ-8) rocket body and the Tiandu-1 cubesat. The three objects were imaged using the Pine Park Observatory on March 22 and 23, 2024 (Fig. 6).
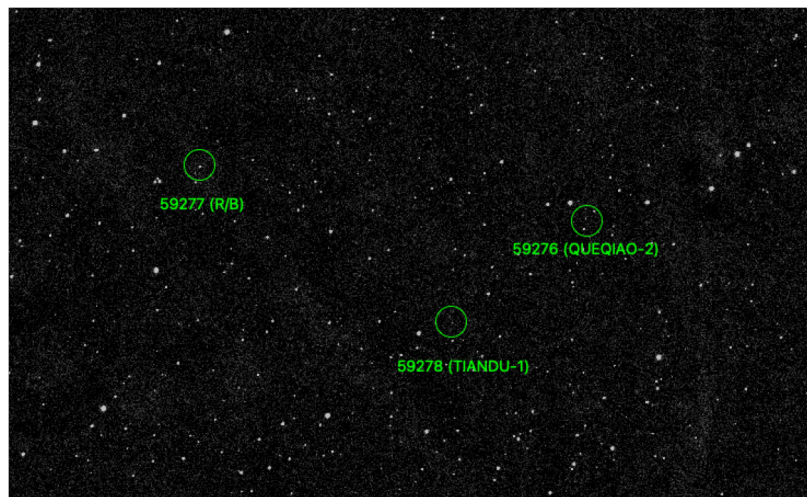

Fig. 6: Queqiao-2 satellite (59276), Chang'e Zheng-8 rocket body (59277), and Tiandu-1 cubesat (59278) imaged on March 23, 2024 from Pine Park Observatory.

On March 22, 2024, only 29 20-second exposure images were collected over a 10-minute period. The Tiandu-1 cubesat was not visible during imaging. On March 23, 2024, there were 80 30-second exposure images collected over a 40-minute period. The results from the algorithm are shown below in Fig. 7.
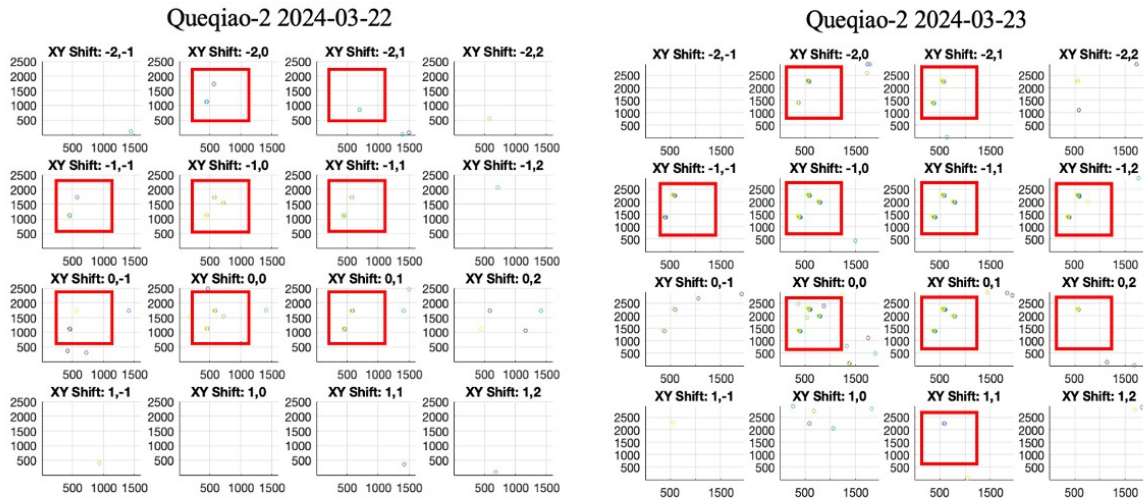

Fig. 7: Sixteen motion hypotheses were applied to the images and detections (highlighted in red) were generated for each night.

All three objects were successfully detected for each night of observations, even for the images where the cubesat was not initially visible, as shown in Fig. 8 below of the cluster detections.
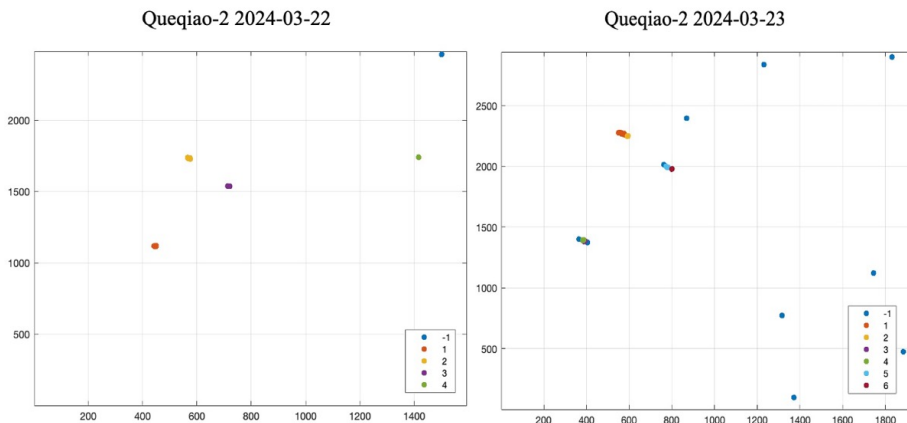

Fig. 8: Clustered detections shown for each night of observations for the three targets.

The parameters used for processing this image set are listed in Table 2.

Table 2: Algorithm parameters used for the Quequiao-2 datasets.

	2024-03-22	2024-03-23
Num. Of Images	29	80
Mask Multiplier	1	1
SNR Threshold	6	6
X Shift Values	[-2:1]	[-2:1]
Y Shift Values	[-1:2]	[-1:2]
Num. Of Stacked Images	10	10
Neighborhood Pixel Search	10	10
Minimum Num. Of Points	5	5

ORION SPACECRAFT

The objective of the Artemis-1 mission was testing the Orion spacecraft, which will be the module responsible for returning humans to the lunar surface. The mission spanned 25 days between November and December 2022 where the Orion spacecraft was inserted into Distant Retrograde Orbit (DRO) then returned to Earth [2]. Observations were collected using the FTN 16-inch telescope on December 10, 2022 during the spacecraft's return to Earth. See Fig. 9 below for example sensor image of Orion.

Fig. 9: The Orion spacecraft imaged on December 10, 2022 using the USAFA's 16-inch telescope.

The Orion spacecraft imagery totaled to 40 15-second exposure images over 15 minutes. The results from the algorithm are shown below in Fig. 10. The spacecraft is moving across the sensor's field of view quickly, as reflected in the detections on the left of Fig. 10, color coded by time, where yellow is the starting position and blue is the ending position. The parameters used for processing this image set are listed in Table 3.
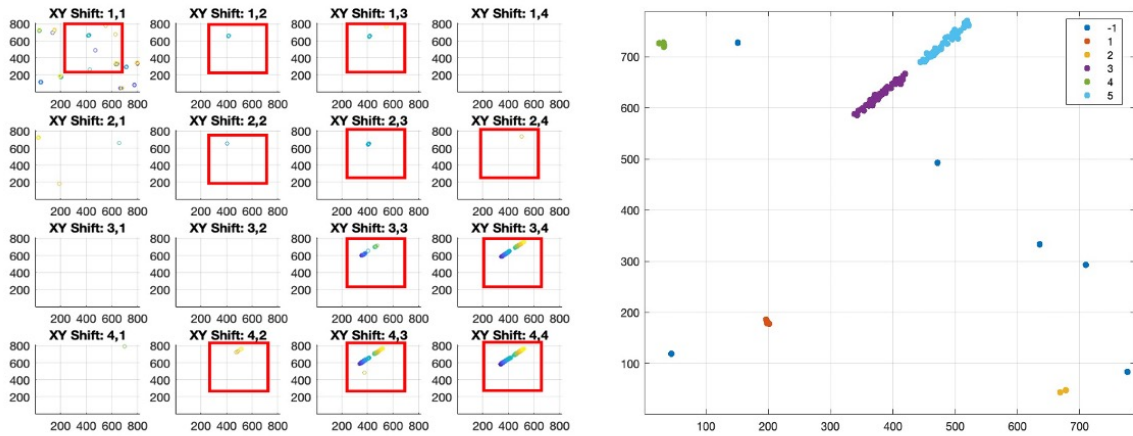
Fig. 10: Graphic on left showing the 16 motion hypotheses applied to the images which shows detections (highlighted in red) across the sequence of images. Clustered detections are shown on the right for the Orion spacecraft.

Table 3: Algorithm parameters used for the Orion spacecraft dataset.

Num. Of Images	40
Mask Multiplier	1
SNR Threshold	6
X Shift Values	[1:4]
Y Shift Values	[1:4]
Num. Of Stacked Images	10
Neighborhood Pixel Search	2
Minimum Num. Of Points	2

LUCY

Lucy is a NASA space probe deployed in October 2021 to explore asteroids within our solar system over the course of 2023-2033 [9]. To date, Lucy has observed one of the eleven target objects with its flyby of the asteroid *Dinkenish* on November 1, 2023. Lucy was imaged using the Pine Park Observatory on October 17, 2021 (Fig. 11).

Fig. 11: The Lucy space probe imaged on October 17, 2021with Pine Park Observatory.

The results of the algorithm are shown below in Fig. 12 while the parameters used are shown in Table 4.
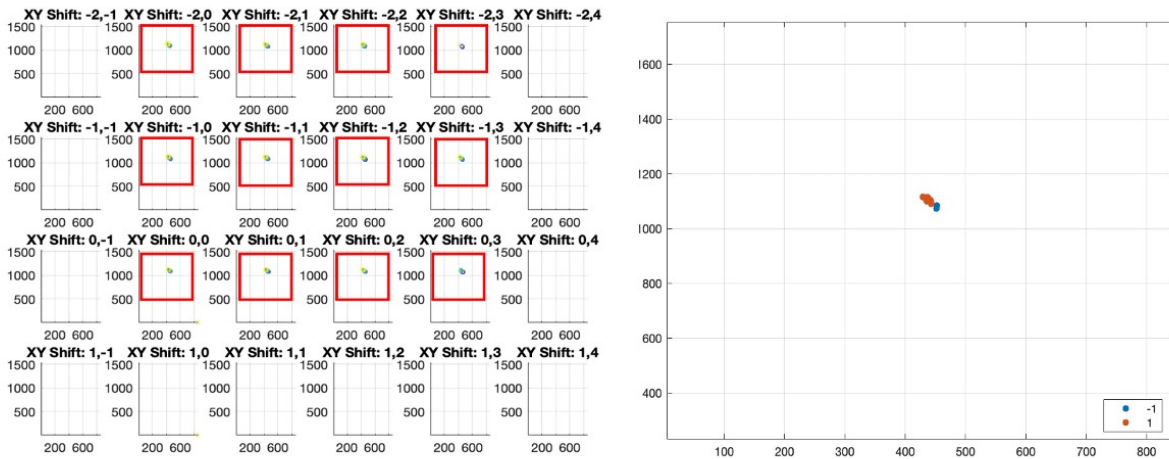

Fig. 12: Algorithm outputs for the Lucy space probe are shown above. The plot on the left shows the detections while the plot on the right is the detection clusters.

Table 4: Algorithm parameters used for the Lucy space probe dataset.

Num. Of Images	50
Mask Multiplier	1
SNR Threshold	6
X Shift Values	[-2:1]
Y Shift Values	[-1:4]
Num. Of Stacked Images	8
Neighborhood Pixel Search	30
Minimum Num. Of Points	2

LUNA-25 FREGAT ROCKET BODY (R/B)

Luna-25 is a failed mission from Roscomos where the lander crashed into the Moon on August 19, 2023 [10]. The Fregat rocket body that delivered Luna-25 to its untimely fate was still in orbit until it decayed in February 2024. Fregat was imaged using Pine Park Observatory on January 28, 2024 (Fig. 13).

Fig. 13: The Fregat rocket body imaged on January 28, 2024 with Pine Park Observatory.

The results of the algorithm are shown below in Fig. 14 while the parameters used are shown in Table 5.
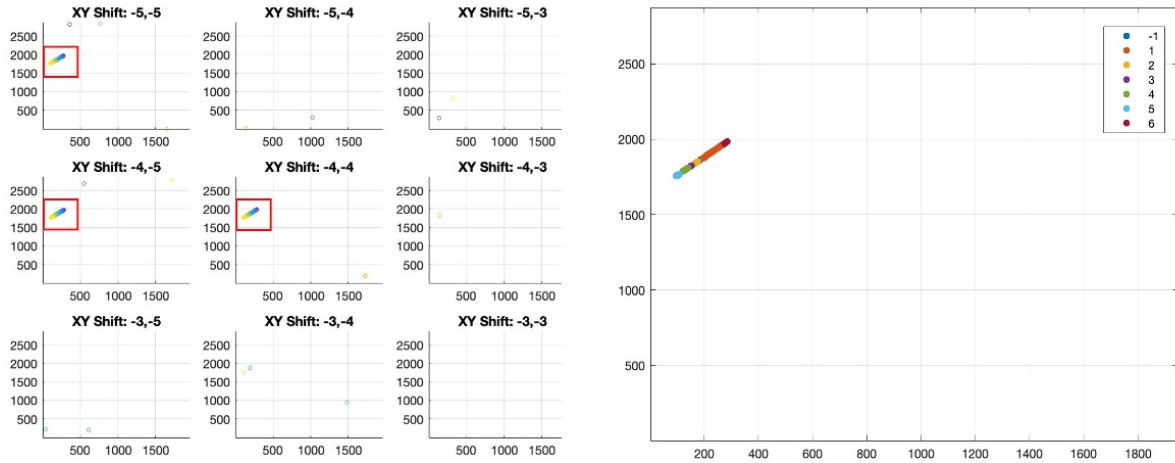
Fig. 14: Algorithm outputs for the Fregat rocket body are shown above. The plot on the left shows the detections while the plot on the right is the detection clusters.

Table 5: Algorithm parameters used for the Fregat rocket body dataset.

Num. Of Images	50
Mask Multiplier	1
SNR Threshold	6
X Shift Values	[-5:-3]
Y Shift Values	[-5:-3]
Num. Of Stacked Images	10
Neighborhood Pixel Search	5
Minimum Num. Of Points	3

In general, all of the cislunar datasets solved using similar algorithm input parameters. The main difference in the algorithm input parameters for this dataset being the motion hypothesis values or the number of stacked images. A generalized set of algorithm input parameters were tested as most of the parameters in the results section is similar. While this generalized set will not necessarily provide the greatest number of detections, it still adequately solves the data sets with the same visual indicators we are looking for when doing the individual parameter inputs. Table 6 lists the generalized input parameters.

Table 6: A universal algorithm input parameter set is listed below after being tested and successfully detecting the target in all of the cislunar datasets.

Num. Of Images	1-50 Images
Mask Multiplier	1
SNR Threshold	6
X Shift Values	[-4:4]
Y Shift Values	[-4:4]
Num. Of Stacked Images	10
Neighborhood Pixel Search	5
Minimum Num. Of Points	3

3.4 ASTEROID DATA

The second set of algorithm test data consists of asteroid imagery. While the intention of the algorithm is to automatically detect cislunar targets, asteroids serve as good targets for more difficult test cases. In general, cislunar objects won't extend past the Moon-Earth L2 Lagrange point at approximately 500,000-kilometers from Earth while asteroids can extend up to 600M kilometers from Earth. Due to the increased distance to the asteroid belt, image collection windows were expanded to multiple hours per object.

ASTEROID 1036 GANYMED

Ganymed is a Near Earth Asteroid (NEA) that is 37-kilometers in diameter, making it one of the largest asteroids. The asteroid is in orbit around 90 million kilometers from Earth. Ganymed was imaged using the Pine Park Observatory on July 6, 2024, as shown in Fig. 15 below.
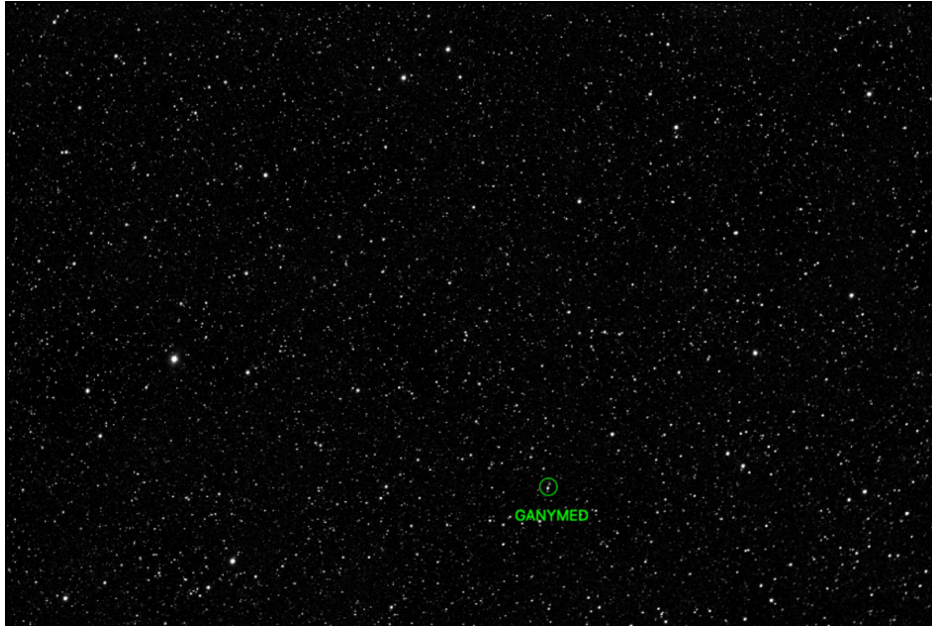

Fig. 15: Asteroid 1036 Ganymed imaged on July 6, 2024 using the Pine Park Observatory.

The results of the algorithm are shown below in Fig. 15 and the parameters used are shown in Table 7. A zoomed-in region of the detections is shown on the right. This dataset is an example of an edge case where the target is moving too little over the sequence of imaging. This subsequently causes the target to be covered when doing the background mask and subtraction. To alleviate this from happening, the image sequence can be decimated using, for example, only every fifth image. This allows for more motion of the object between each selected image so it is not discarded during background image subtraction.
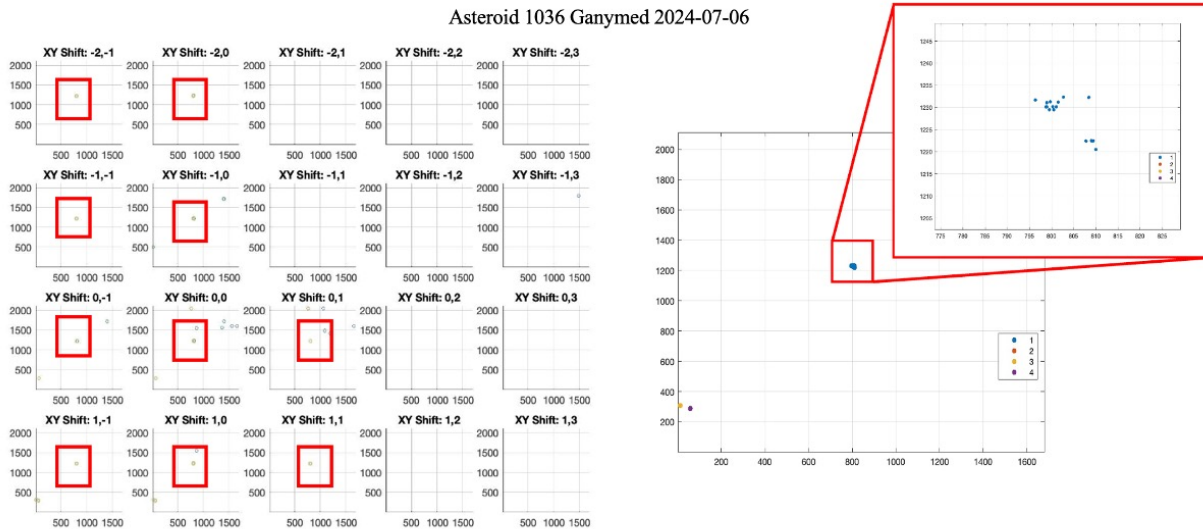
Fig. 16: Algorithm outputs for Asteroid 1036 Ganymed are shown above. The plot on the left shows the detections while the plot on the right is the detection clusters.

Table 7: Algorithm parameters used for the Asteroid 1036 Ganymed dataset.

Num. Of Images	12
Mask Multiplier	4
SNR Threshold	8
X Shift Values	[-2:1]
Y Shift Values	[-1:3]
Num. Of Stacked Images	4
Neighborhood Pixel Search	2
Minimum Num. Of Points	2

4. SUMMARY

The asteroid detection algorithm we implemented for automatically finding cislunar spacecraft in images taken with ground-based optical observatories was fairly successful. This process is still a prototype but provides advantages compared to the original method of detecting targets through tedious manual processing. This method, which provides the user a list of targets that are the likely non-stellar, along with multiple graphics to locate targets, is ideal in situations where the target is in a field of view with many stars, like imaging near the Milky Way band.

We demonstrated a clear performance increase when adding in the shift and median combination image processing method as opposed to only a background subtraction, allowing for dimmer targets to collect more signal for detection. Additionally, this algorithm was tested on sets of images containing asteroids which are more difficult to detect than cislunar spacecraft due to the increased ranges and limited target signal. The algorithm was able to successfully extract the various asteroids in the images for both of the example image sets.

Improvements have been identified for future work on this algorithm. The algorithm parameters should be explored in-depth for varying collection contexts. The algorithm could also complete a more precise velocity search though implementing a closed-loop optimization process to find the ideal target motion shift value. Determining the optimal velocity search would maximize the target signal. Our visual graphics also currently do not overlay the detection indicators on the stacked images, only on the original, single, images. An improvement would be to layer the detections over the stacked frames to visually resolve dimmer targets. Finally, using specific target rates to create the background

image used for subtraction would provide better results compared to solely relying on a median combination of the frames, and would account for any tracking nuances not covered by the alignment of frames.

One highlight of this algorithm is that it works on existing systems with no requirements except for the images to be taken using a sidereal tracking mode (which is a preset in practically every commercial telescope mount) and to have images taken over a long enough period of time to allow for enough movement of the target to happen relative to the sensor. Using the parameters highlighted in this paper, the algorithm processing time is on the order of minutes and allows for a simple way for observers to locate targets in imagery. Additionally, it was tested on different systems including small commercial sized telescopes like Pine Park Observatory and the USAFA FTN 16-inch telescope.

REFERENCES

[1] NASA Office of Inspector General. *Audit of NASA's CLPS Commercial Lunar Payload Services Initiative*, 2024.

[2] Lockheed Martin. Artemis I: One Year Later. https://www.lockheedmartin.com/en-us/news/features/2023/celebrating-the-past–artemis-i-and-orion–one-year-later.html/, November 2023.

[3] M. J. Holzinger. A Primer on Cislunar Space, May 2021. https://www.afrl.af.mil/Portals/90/Documents/RV/A

[4] . Two-Line Element Set (TLE): Format Overview. https://ensatellite.com/tle/, 2023.

[5] K. Raub. XGEO Collection Methods Using New Satellite Observing Techniques on the James Webb Space Telescope. https://amostech.com/TechnicalPapers/2022/Poster/Raub.pdf, September 2022.

[6] K. Raub. XGEO Spacecraft Observation Methods Using Ground-Based Optical Telescopes. https://amostech.com/TechnicalPapers/2023/Poster/Raub.pdf, September 2023.

[7] T. Yanagisawa. Automatic Detection Algorithm for Small Moving Objects. *Astronomical Society of Japan*, 2005.

[8] NASA. Queqiao-2. https://nssdc.gsfc.nasa.gov/nmc/spacecraft/display.action?id=QUEQIAO-2, March 2024.

[9] NASA. Lucy Science Goals. https://science.nasa.gov/mission/lucy/science/, April 2024.

[10] A. Jones. Luna-25 crashes into moon after orbit maneuver. https://spacenews.com/luna-25-crashes-into-moon-after-orbit-maneuver/, August 2023.